



Supplement of

The effect of temperature-dependent material properties on simple thermal models of subduction zones

Iris van Zelst et al.

Correspondence to: Iris van Zelst (iris.vanzelst@dlr.de, iris.v.zelst@gmail.com)

The copyright of individual parts of the supplement might differ from the article licence.

S1. Subduction community benchmark by van Keken et al. (2008)

Here, we present the results of xFieldstone for the five cases of the community benchmark by van Keken et al. (2008) plus one additional case where we combine the diffusion and dislocation rheologies. The details of the benchmark are outlined in van Keken et al. (2008) and the methods of xFieldstone can be found in the main text. Here, we briefly summarise the different cases, adhering to the numbering coined in van Keken et al. (2008). Case 1a is an analytical corner flow model based on the analytical solution by Batchelor (1967) (Figure S1). Case 1b solves for the velocity field in the wedge with an isoviscous rheology with the boundary conditions prescribed by the analytical solution of Batchelor (1967) (Figure S2). Case 1c also has an isoviscous wedge, but has natural boundary conditions for stress at the in- and outflow boundaries of the wedge (Figure S3). For cases 1a - 1c, we run 4 models per case with a uniform grid size of 10 km, 5 km, 2.5 km, and 1.25 km, respectively. We choose these resolutions such that the corner point at $x = 50$ km and $y = 550$ km is accurately represented in the grid. Figure S4 shows the results of xFieldstone for the isoviscous cases in comparison to the results from van Keken et al. (2008).

Case 2a uses the same boundary conditions as case 1c, but considers a diffusion creep rheology instead of an isoviscous model (Figure S5). Case 2b has a dislocation rheology (Figure S6). We add an additional case called case 2c where we combine diffusion and dislocation creep, assuming two viscous dampers in series (Figure 4). In practice, dislocation creep is dominant in the upper mantle that we consider here, which results in very similar model diagnostics between case 2b and case 2c (Figure S7). However, the complete fields of the model do show differences in the mantle wedge.

For cases 2a - 2c, we run 3 models per case with a uniform grid size of 10 km, 5 km and 2.5 km. We are not able to run the model at any higher resolutions, due to limits on the memory necessary. Figure S7 shows the results for xFieldstone for the temperature-dependent rheologies combined with the data from van Keken et al. (2008).

All in all, xFieldstone reproduces the cases of van Keken et al. (2008) well and obtains similar model diagnostics to the codes presented in van Keken et al. (2008).

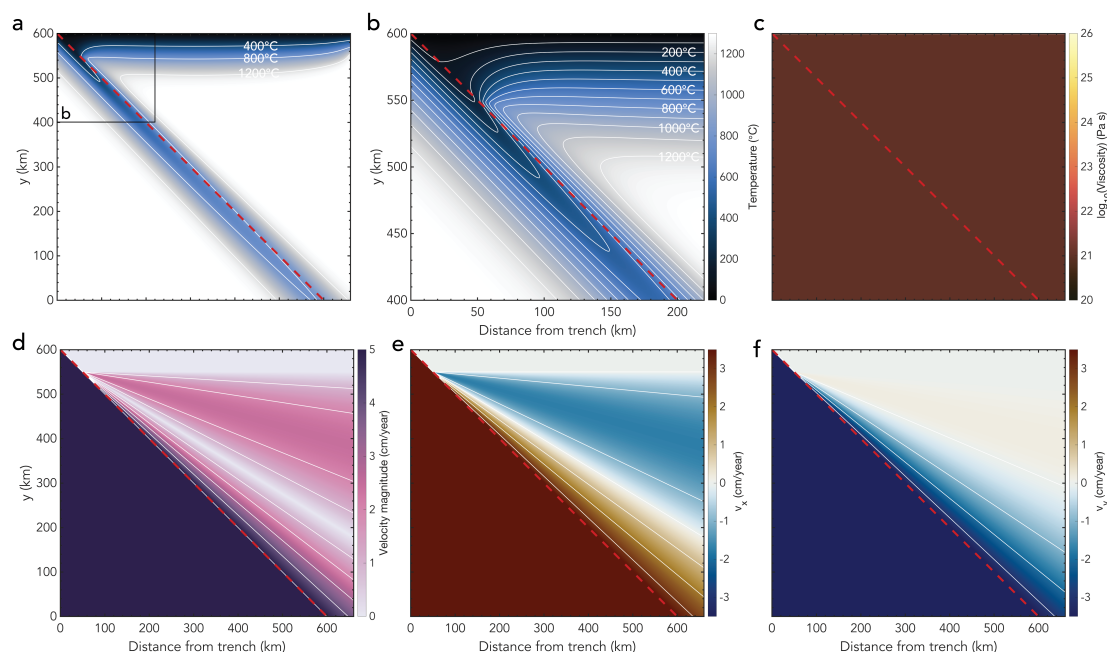


Figure S1: Case 1a: Analytical cornerflow model. (a) Temperature field with isotherms indicated in white; (b) zoom of the temperature field; (c) viscosity with white contours for $\eta = 10^{20}$ Pa s to $\eta = 10^{26}$ Pa s with intervals of one order magnitude (note: for case 1a the viscosity is constant, so there are no visible contours); (d) velocity magnitude with white contours for $v = 0$ cm/year to $v = 5$ cm/year with intervals of 1 cm/year; (e) horizontal component of the velocity with white contours for $v_x = -3$ cm/year to $v_x = 3$ cm/year with intervals of 1 cm/year; (f) vertical component of the velocity with white contours for $v_y = -3$ cm/year to $v_y = 3$ cm/year with intervals of 1 cm/year. The red dashed line indicates the top of the subducting slab.

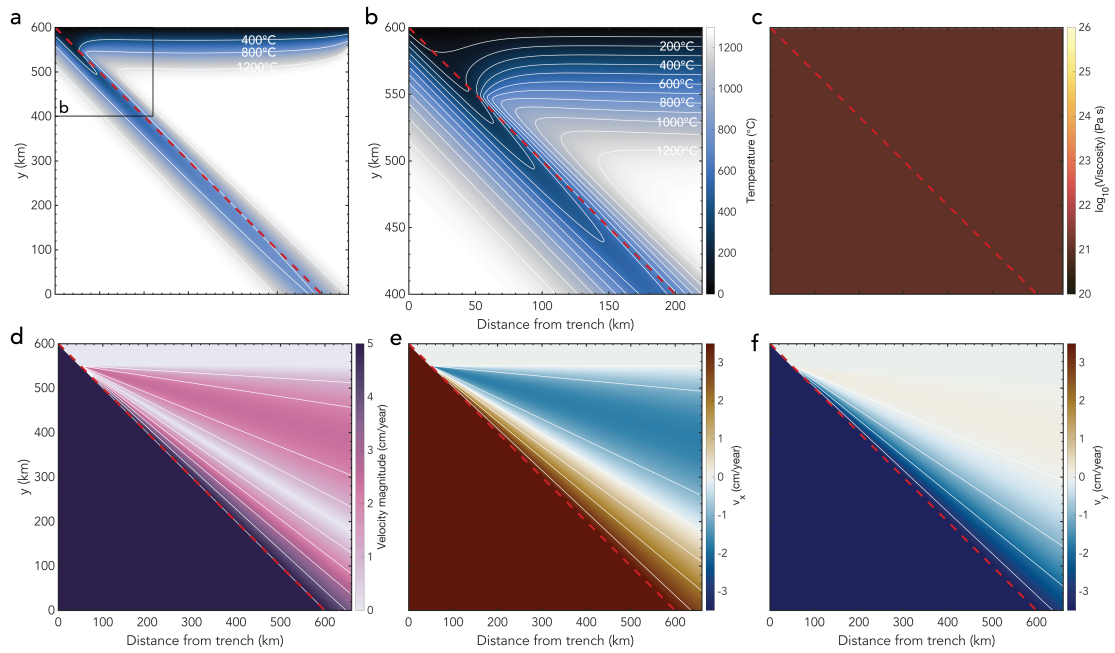


Figure S2: Case 1b: Dynamical flow in an isoviscous wedge I. See the caption of Figure S1 for an explanation of the different panels.

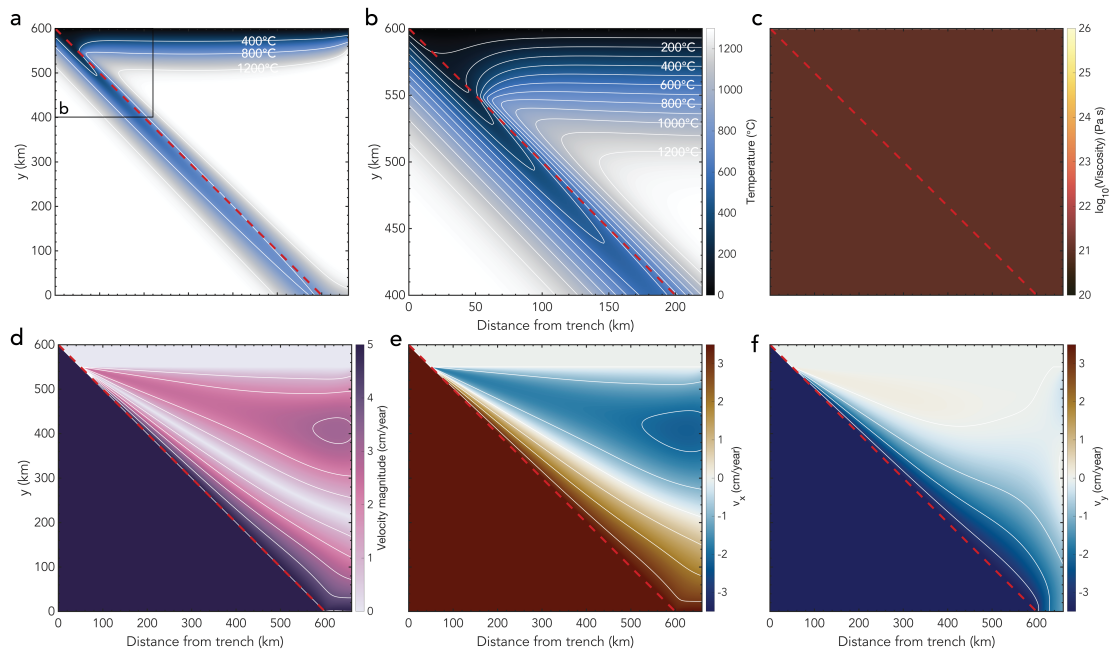


Figure S3: Case 1c: Dynamical flow in an isoviscous wedge II. See the caption of Figure S1 for an explanation of the different panels.

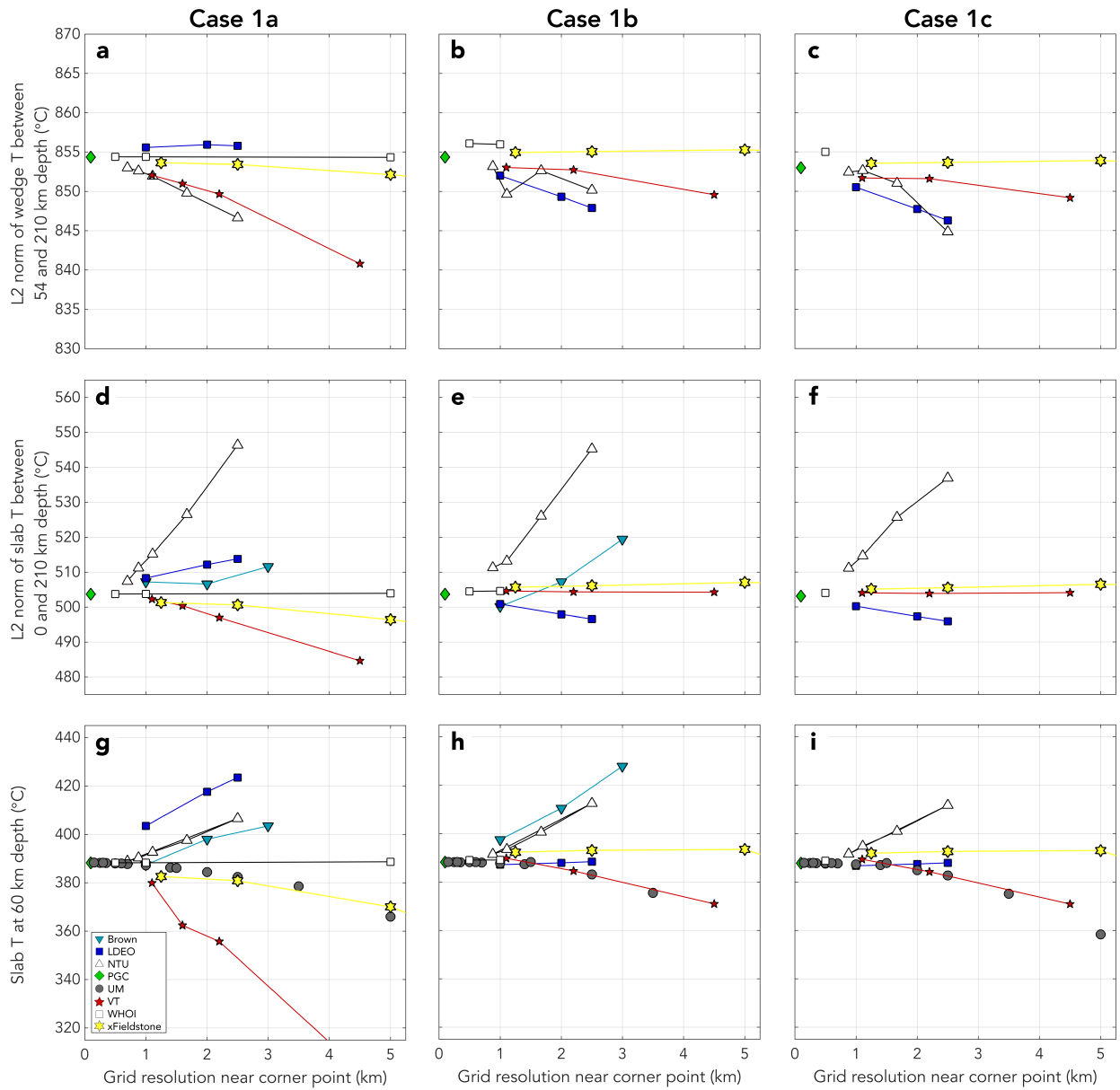


Figure S4: Model diagnostics with different resolutions for (a,d,g) Case 1a: Analytical cornerflow model; (b,e,h) Case 1b: Dynamical flow in an isoviscous wedge I; and (c,f,i) Case 1c: Dynamical flow in an isoviscous wedge II. Data from codes other than xFieldstone is taken from van Keken et al. (2008).

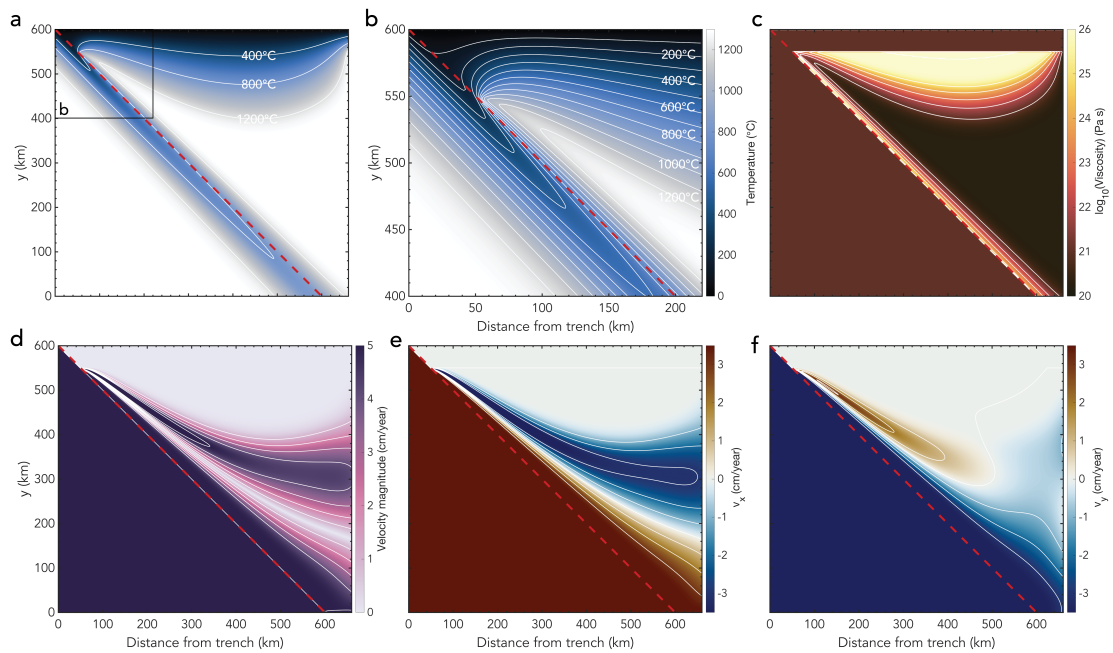


Figure S5: Case 2a: Dynamical flow with a diffusion creep rheology. See the caption of Figure S1 for an explanation of the different panels.

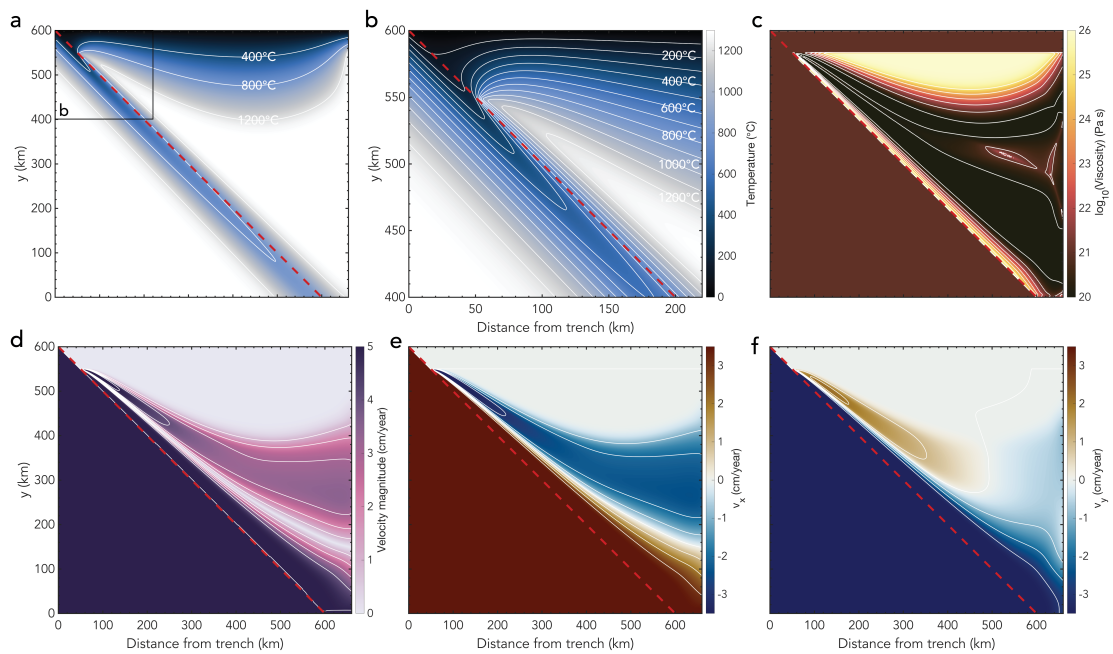


Figure S6: Case 2b: Dynamical flow with a dislocation creep rheology. See the caption of Figure S1 for an explanation of the different panels.

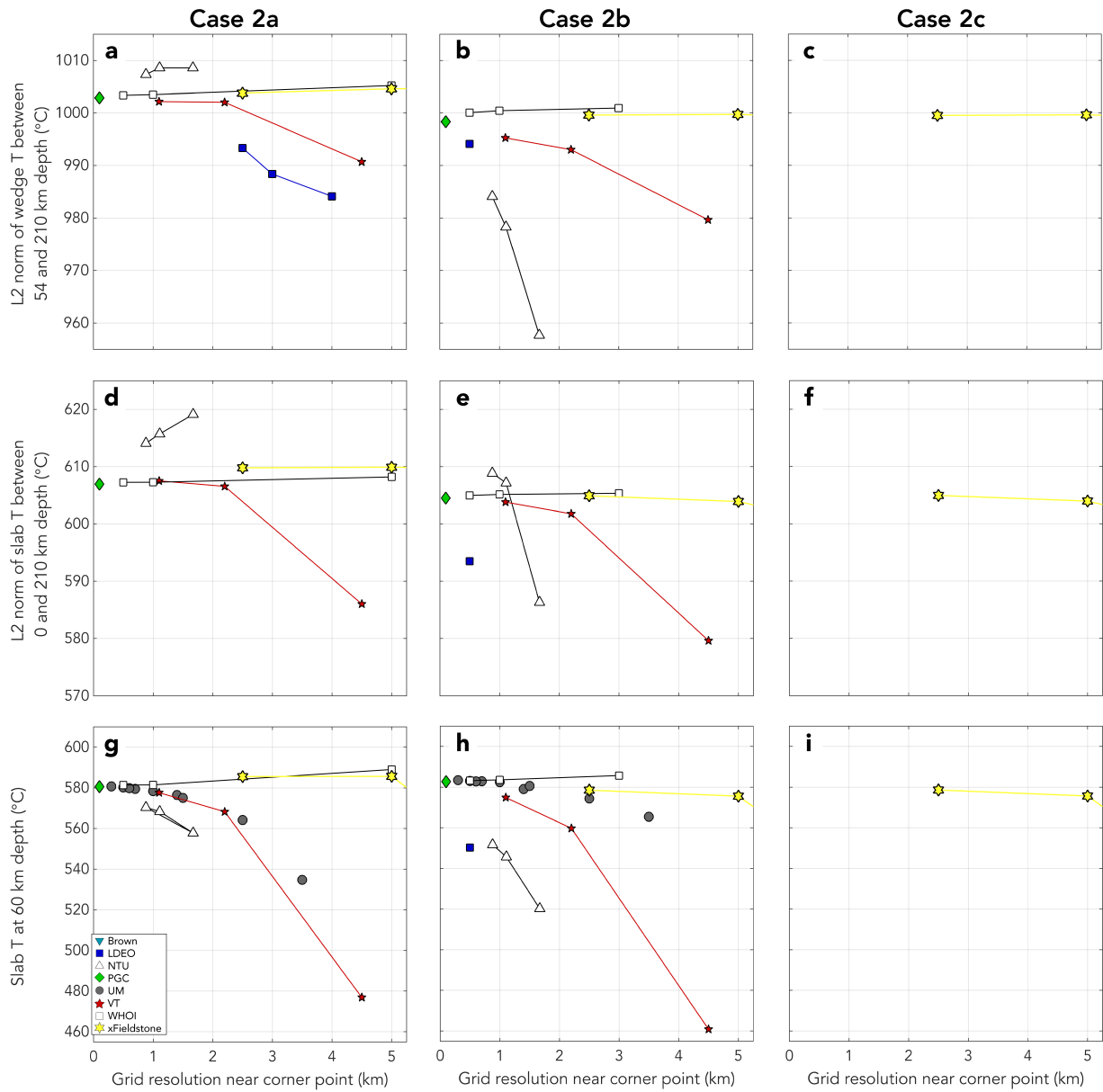


Figure S7: Model diagnostics with different resolutions for (a,d,g) Case 2a: Dynamical flow with a diffusion creep rheology; (b,e,h) Case 2b: Dynamical flow with a dislocation creep rheology; and (c,f,i) Case 2c: Dynamical flow with both a dislocation and diffusion creep rheology. Data from codes other than xFieldstone is taken from van Keken et al. (2008).

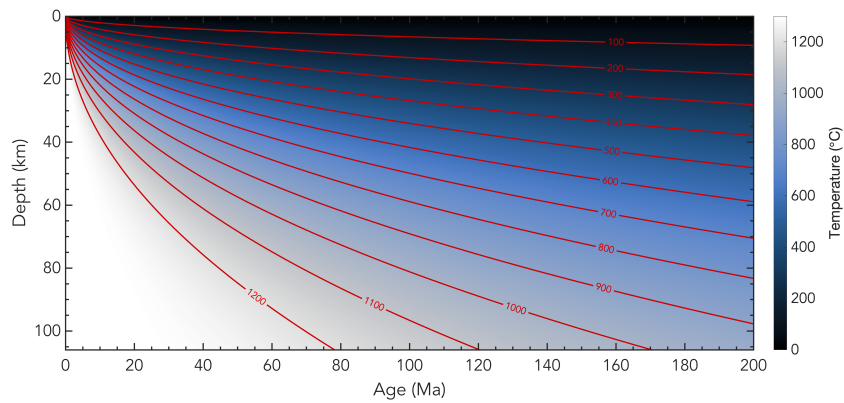


Figure S8: Half-space cooling model. The temperature profile at $t = 50$ Myr is used as the left boundary condition for the top 106 km (i.e., the lithosphere thickness) in model case2c_PvK(_mc). The temperature profiles at $t = 20$ Myr and $t = 80$ Myr are used for models case2c_20PvK and case2c_80PvK, respectively.

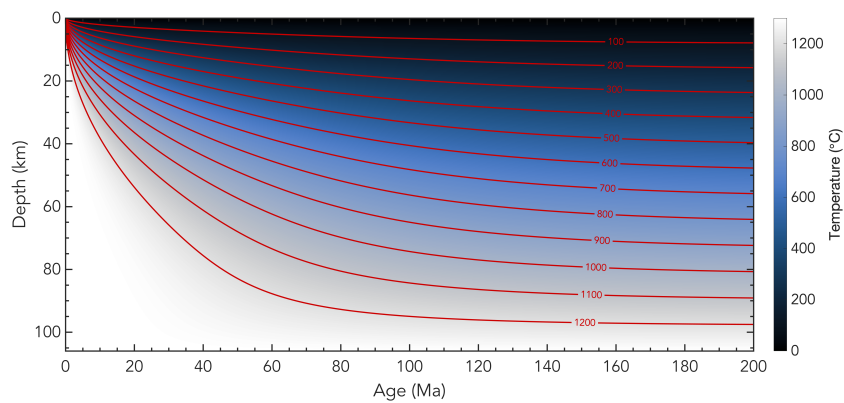


Figure S9: Plate model with constant thermal parameters. The temperature profile at $t = 50$ Myr is used as the left boundary condition for case2c_bc(_mc).

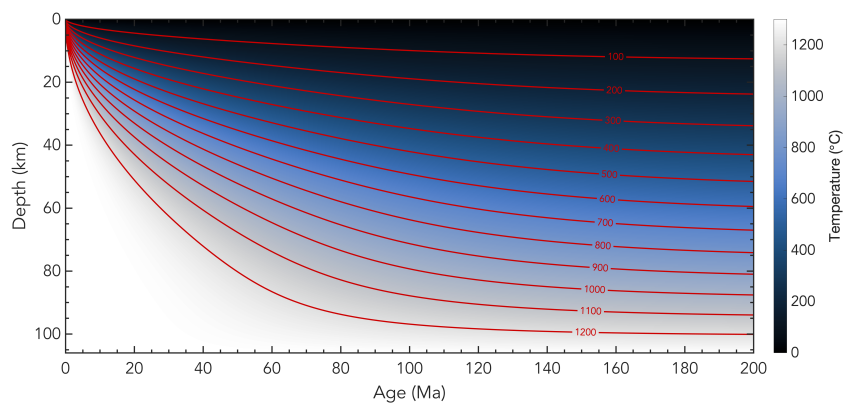


Figure S10: Plate model with a temperature-dependent thermal conductivity according to the approximation of Hofmeister (1999) by McKenzie et al. (2005). The temperature profile at $t = 50$ Myr is used as the left boundary condition for case2c_k1(_mc).

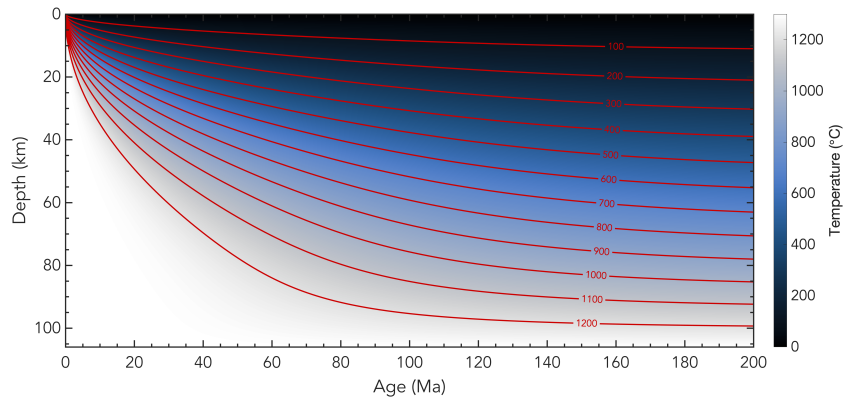


Figure S11: Plate model with a temperature-dependent thermal conductivity according to Xu et al. (2004). The temperature profile at $t = 50$ Myr is used as the left boundary condition for case2c_k2(_mc).

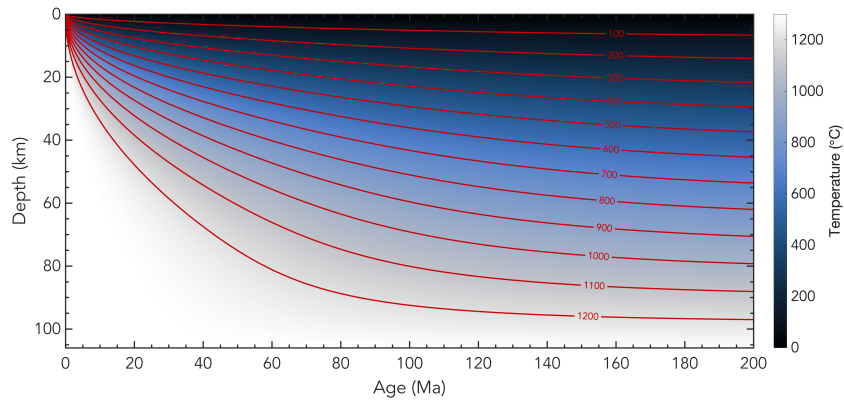


Figure S12: Plate model with a temperature-dependent heat capacity assuming 89% forsterite with values from Berman and Aranovich (1996). The temperature profile at $t = 50$ Myr is used as the left boundary condition for case2c_Cp6(_mc).

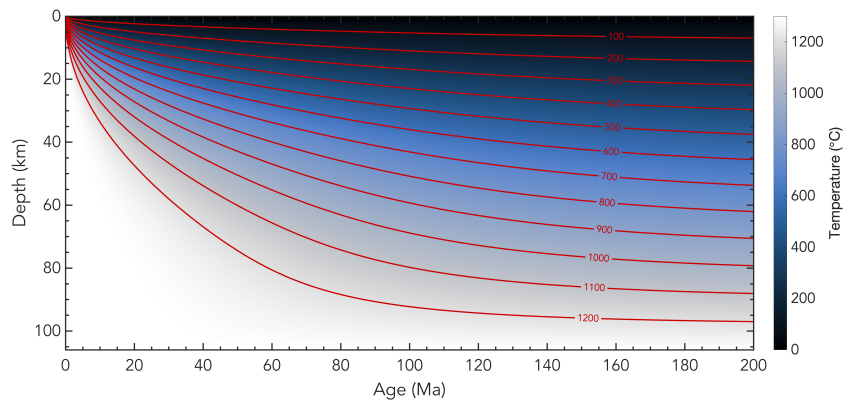


Figure S13: Plate model with a temperature-dependent heat capacity assuming 89% forsterite with values from Berman (1988). The temperature profile at $t = 50$ Myr is used as the left boundary condition for case2c_Cp3(_mc).

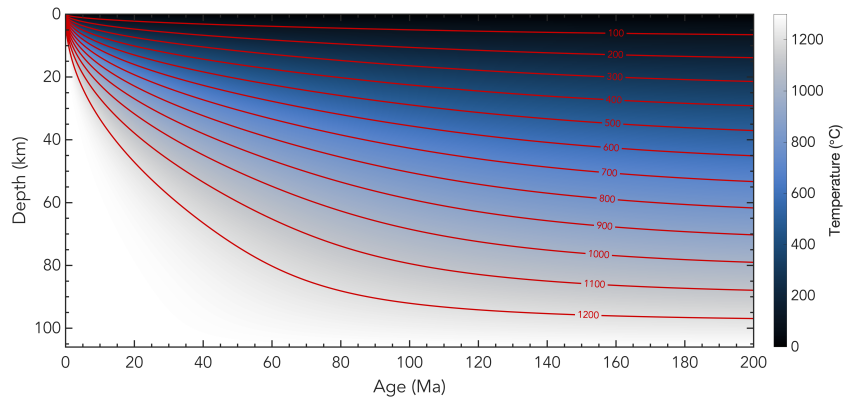


Figure S14: Plate model with a temperature-dependent heat capacity assuming 100% forsterite with values from Berman and Aranovich (1996). The temperature profile at $t = 50$ Myr is used as the left boundary condition for case2c_Cp4(_mc).

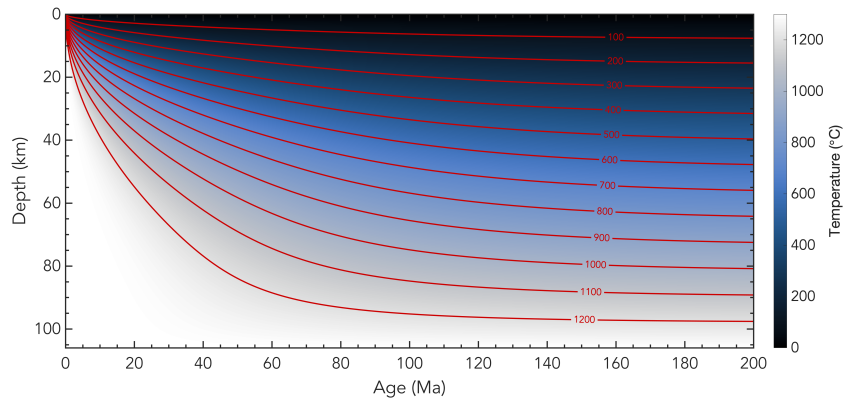


Figure S15: Plate model with a temperature-dependent heat capacity assuming 100% fayalite with values from Berman and Aranovich (1996). The temperature profile at $t = 50$ Myr is used as the left boundary condition for case2c_Cp5(_mc).

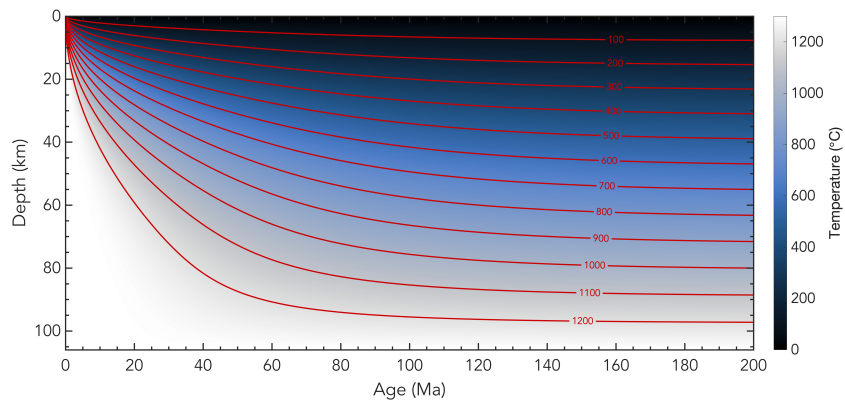


Figure S16: Plate model with a temperature-dependent density according to the parameterisation of Bouhifd et al. (1996) by McKenzie et al. (2005). The temperature profile at $t = 50$ Myr is used as the left boundary condition for case2c_rho(_mc).

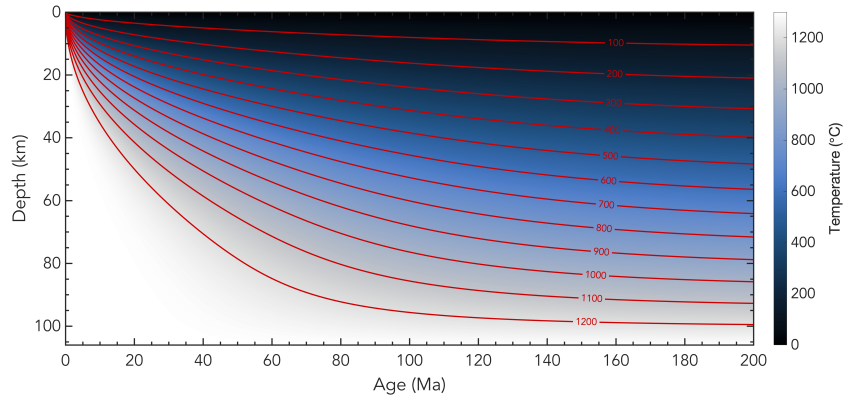


Figure S17: Plate model with a temperature-dependent thermal conductivity according to the approximation of Hofmeister (1999) by McKenzie et al. (2005); a temperature-dependent heat capacity assuming 89% forsterite with values from Berman and Aranovich (1996); and a temperature-dependent density according to the parameterisation of Bouhifd et al. (1996) by McKenzie et al. (2005). The temperature profile at $t = 50$ Myr is used as the left boundary condition for case2c.all(_mc). The temperature profiles at $t = 20$ Myr and $t = 80$ Myr are used for models case2c.20all and case2c.80all, respectively.

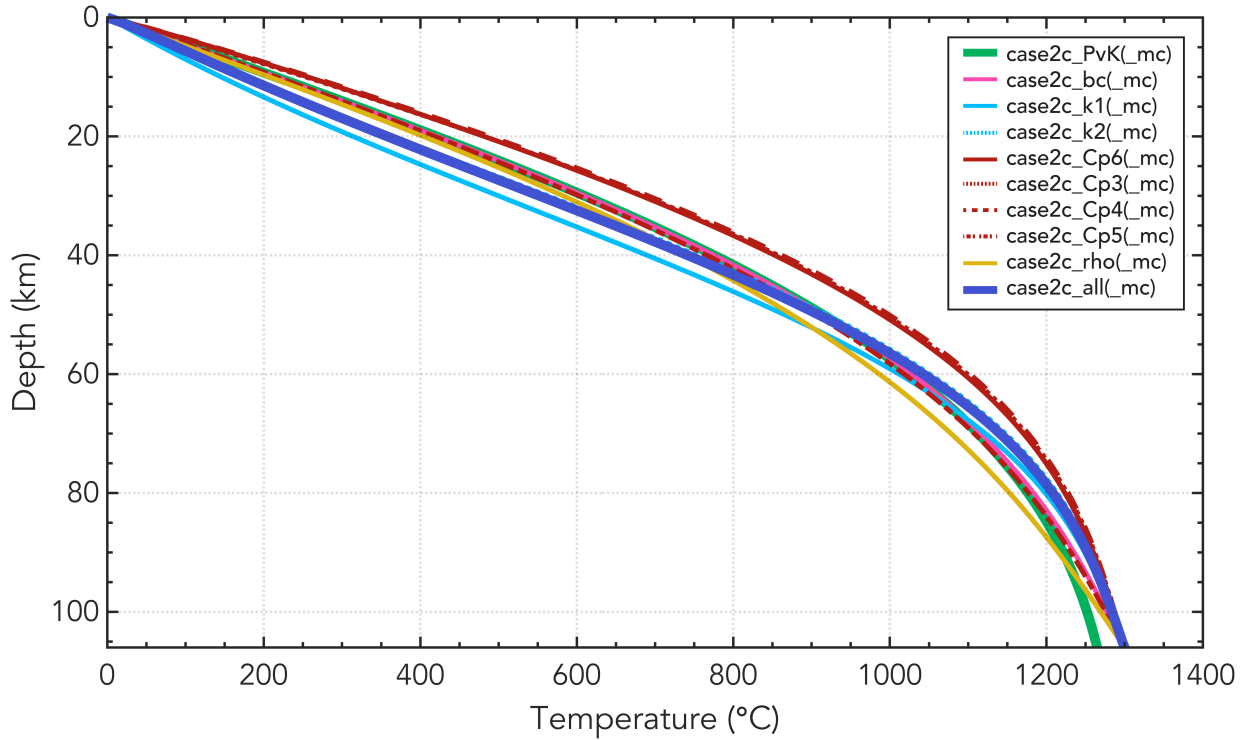


Figure S18: Different temperature boundary conditions for the models listed in Table 1 with an oceanic plate age of 50 Myr at the left side of the model for the top 106 km of the model (i.e., the oceanic lithosphere thickness), below which the temperature is constant at $T = 1300^\circ\text{C}$.

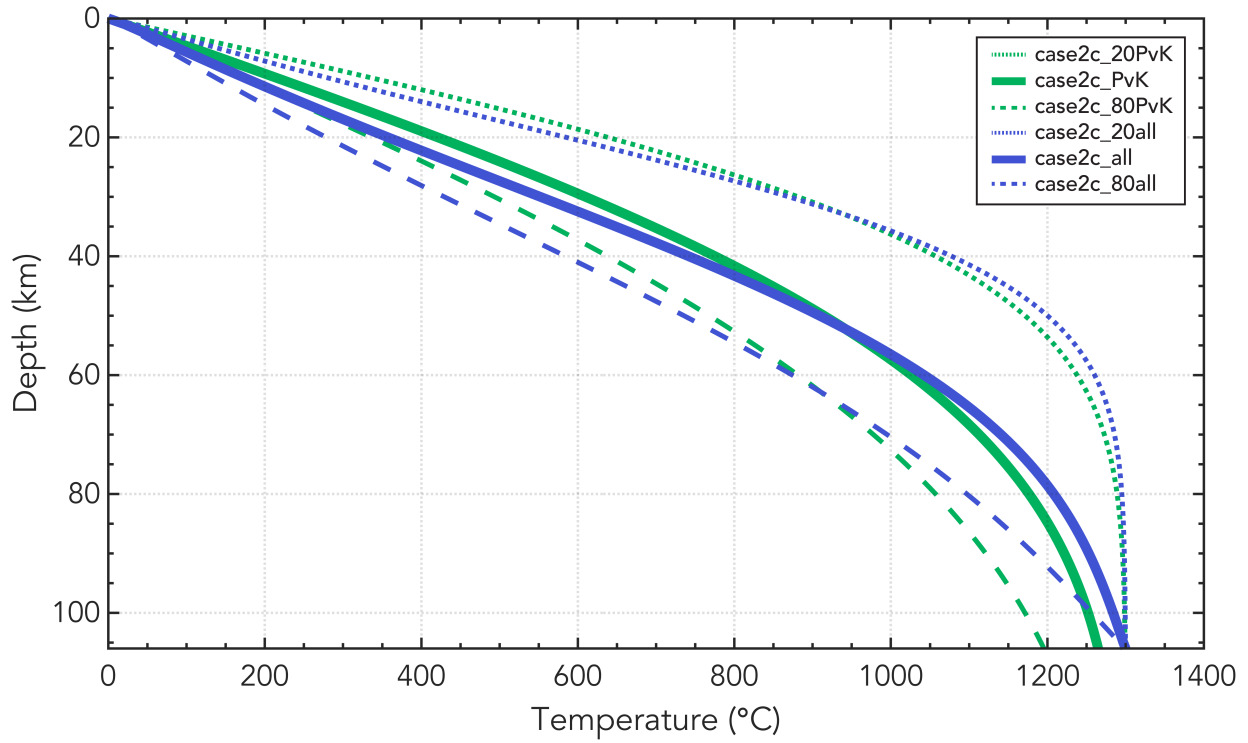


Figure S19: Different temperature boundary conditions for the models case2c_PvK and case2c_all listed in Table 1 with different plate ages of 20, 50, and 80 Myr at the left side of the model for the top 106 km of the model (i.e., the oceanic lithosphere thickness), below which the temperature is constant at $T = 1300^{\circ}\text{C}$.

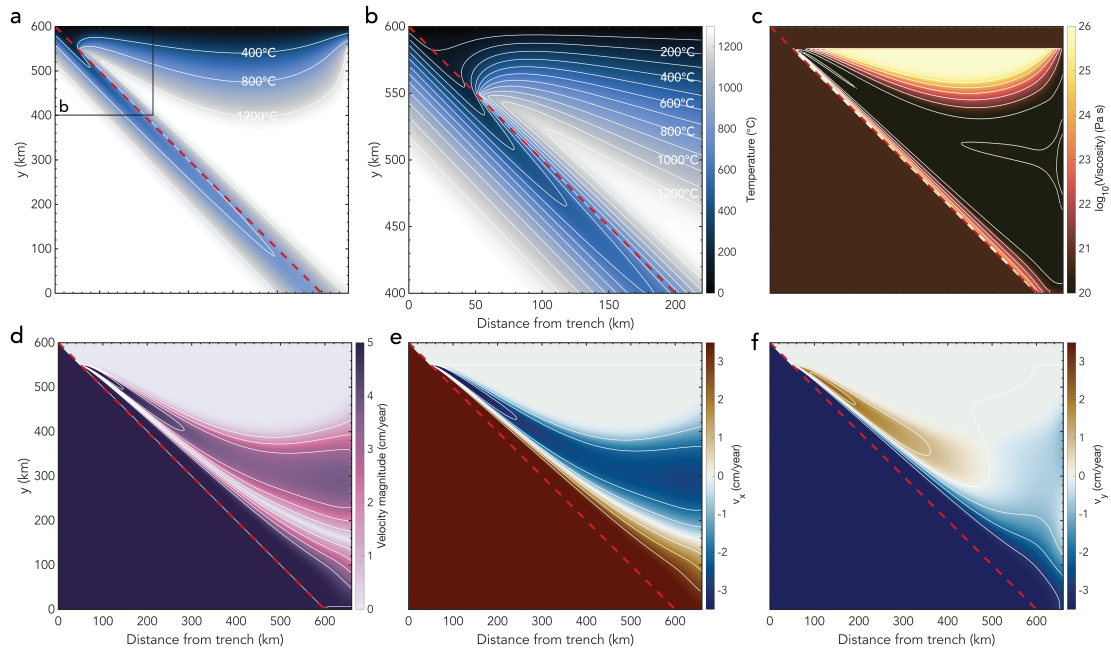


Figure S20: Model case2c_bc with constant thermal parameters according to van Keken et al. (2008) and the plate model as the left temperature boundary condition. See the caption of Figure S1 for an explanation of the different panels.

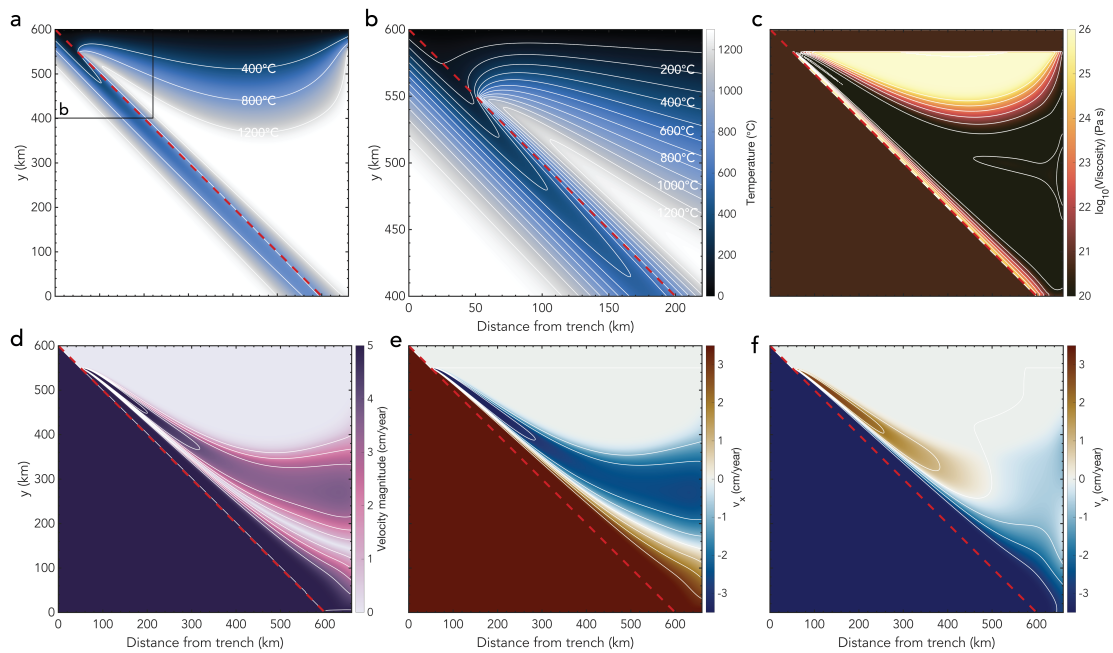


Figure S21: Model case2c_k1 with temperature-dependent thermal conductivity according to the approximation of Hofmeister (1999) by McKenzie et al. (2005). See the caption of Figure S1 for an explanation of the different panels.

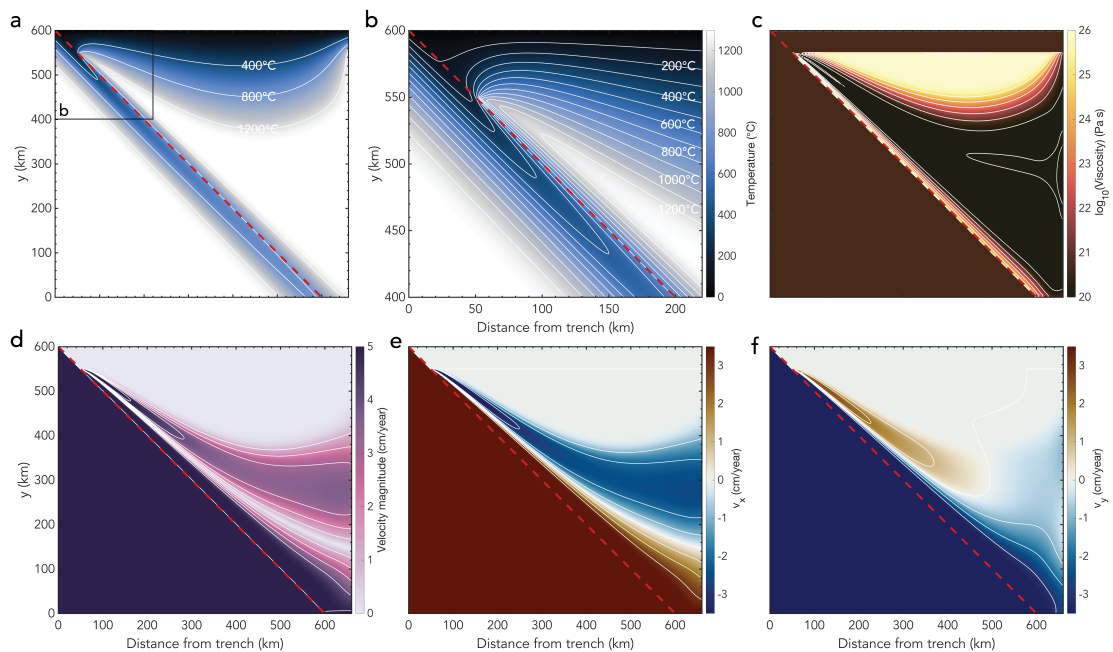


Figure S22: Model case2c_k2 with temperature-dependent thermal conductivity according to Xu et al. (2004). See the caption of Figure S1 for an explanation of the different panels.

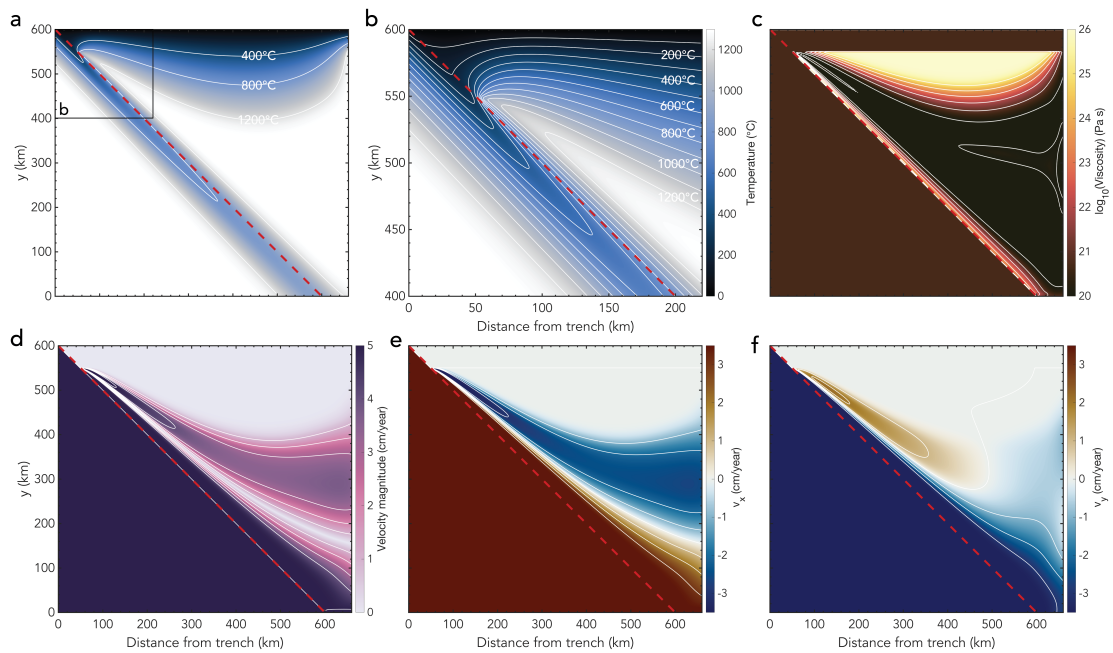


Figure S23: Model case2c_Cp6 with temperature-dependent heat capacity assuming 89% forsterite and values from Berman and Aranovich (1996). See the caption of Figure S1 for an explanation of the different panels.

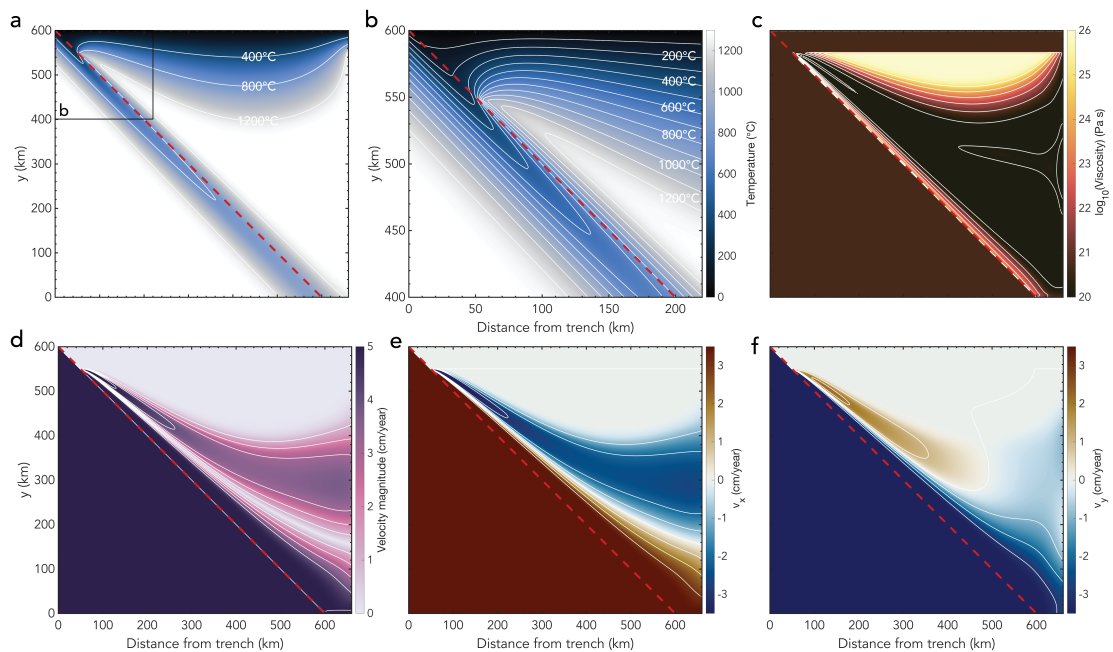


Figure S24: Model case2c_Cp3 with temperature-dependent heat capacity assuming 89% forsterite and values from Berman (1988). See the caption of Figure S1 for an explanation of the different panels.

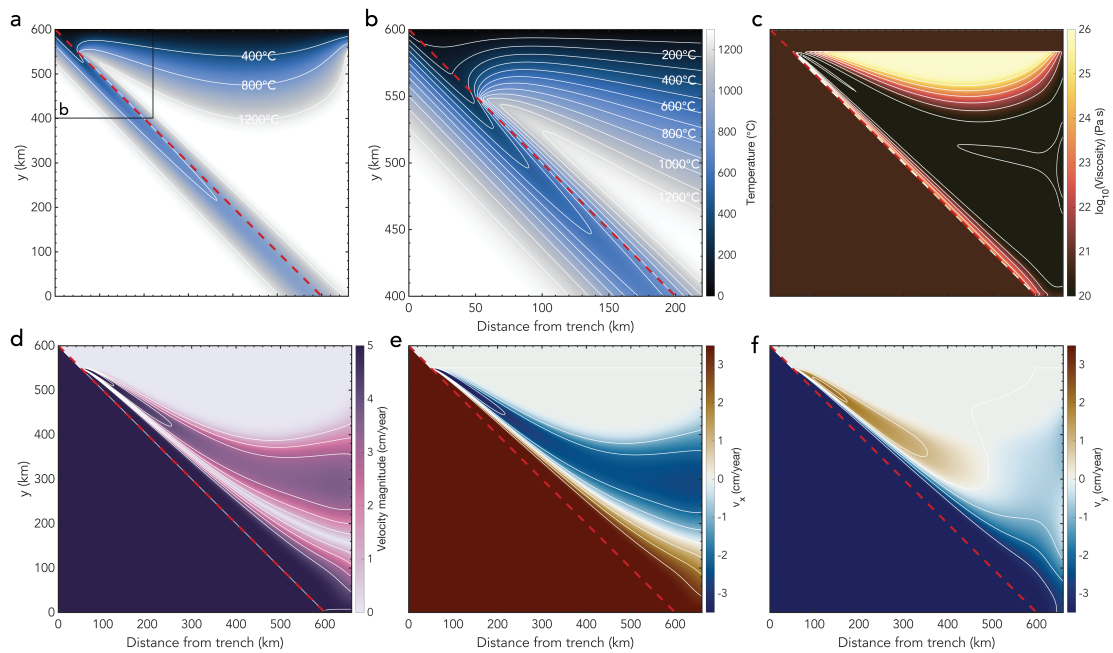


Figure S25: Model case2c_Cp4 with temperature-dependent heat capacity assuming 100% forsterite and values from Berman and Aranovich (1996). See the caption of Figure S1 for an explanation of the different panels.

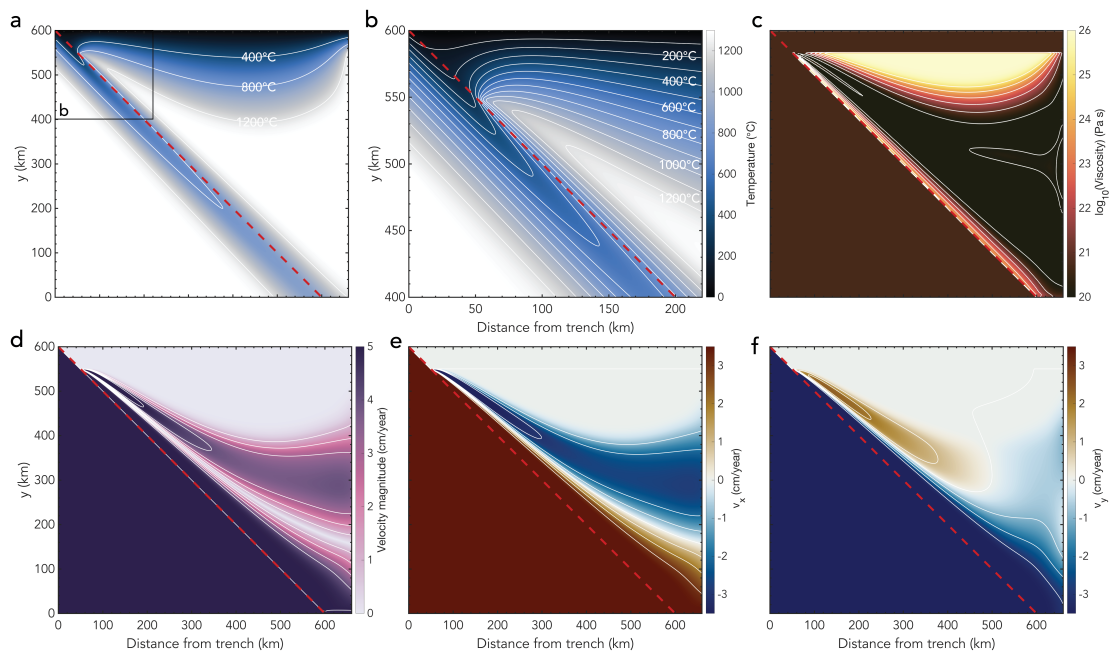


Figure S26: Model case2c_Cp5 with temperature-dependent heat capacity assuming 100% fayalite and values from Berman and Aranovich (1996). See the caption of Figure S1 for an explanation of the different panels.

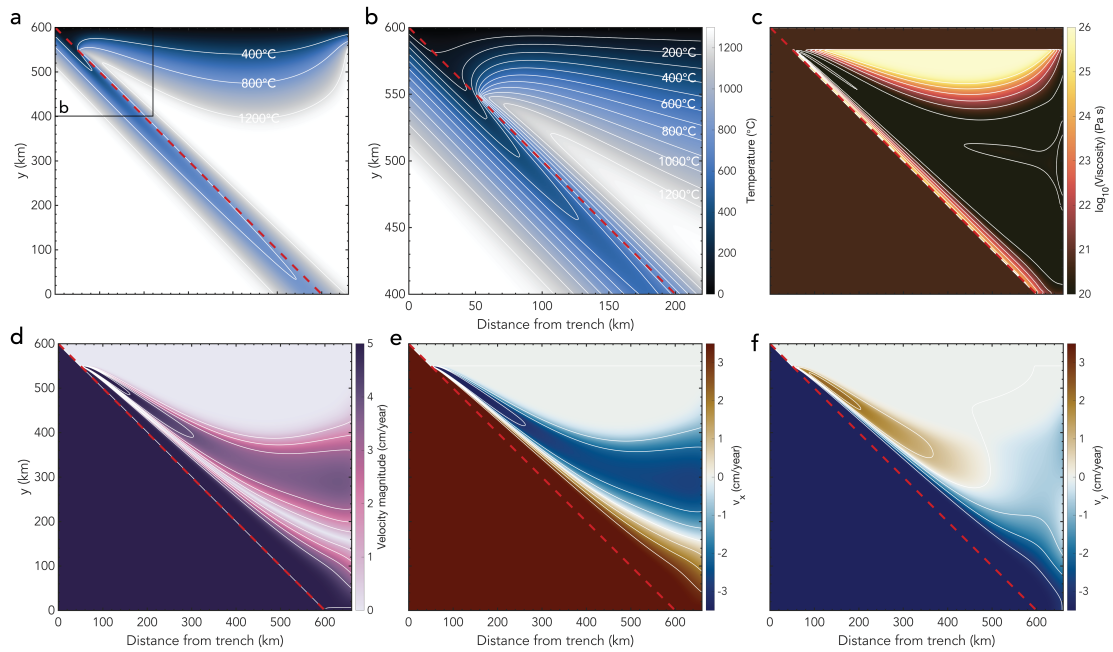


Figure S27: Model case2c_rho with temperature-dependent density according to the approximation of Bouhfid et al. (1996) by McKenzie et al. (2005). See the caption of Figure S1 for an explanation of the different panels.

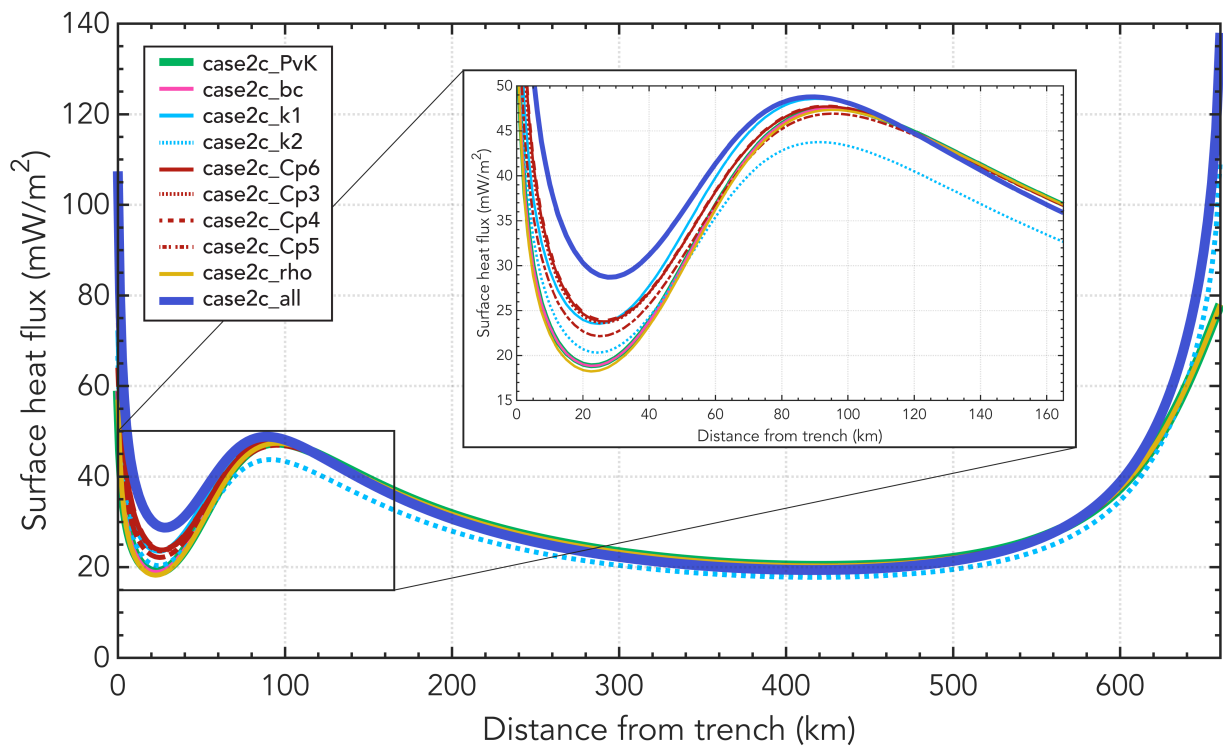


Figure S28: The surface heat flux for the models with an oceanic plate age of 50 Myr without the crustal parameterisation (Table 1). The zoom set-in shows the detailed heat fluxes near the trench.

Table S1: Model diagnostics (continued from main article)

	$T_{x=60\text{km}}$ (°C)	T_{slab} (°C)	T_{wedge} (°C)	Max depth 350°C (km)	Max depth 450°C (km)	Max depth 600°C (km)
case2c_PvK_mc	625.7	645.3	1006.2	83.8	125.0	232.5
case2c_bc_mc	662.0	684.2	1011.9	61.3	82.5	156.3
case2c_k1_mc	607.8	632.9	959.9	76.3	116.3	232.5
case2c_k2_mc	633.7	654.3	986.9	70.0	102.5	201.3
case2c_Cp6_mc	692.8	715.4	1018.9	52.5	68.8	117.5
case2c_Cp3_mc	693.5	716.3	1019.1	52.5	68.8	116.3
case2c_Cp4_mc	695.8	717.4	1021.6	52.5	68.8	116.3
case2c_Cp5_mc	661.0	695.1	990.3	55.0	71.3	127.5
case2c_rho_mc	650.1	673.1	1004.6	63.8	88.8	171.3
case2c_all_mc	628.8	655.3	959.8	65.0	93.8	185.0
case2c_PvK_op	635.9	651.6	1018.3	83.8	123.8	230.0
case2c_bc_op	673.6	691.6	1024.5	61.3	81.3	153.8
case2c_k1_op	619.9	640.3	975.4	75.0	115.0	228.8
case2c_k2_op	645.1	661.4	1001.3	68.8	101.3	198.8
case2c_Cp6_op	705.3	723.4	1031.7	51.3	67.5	115.0
case2c_Cp3_op	706.0	724.3	1031.9	51.3	67.5	115.0
case2c_Cp4_op	708.2	725.3	1034.4	51.3	67.5	113.8
case2c_Cp5_op	674.9	703.8	1003.8	52.5	70.0	125.0
case2c_rho_op	661.9	680.5	1017.3	62.5	87.5	168.8
case2c_all_op	642.0	663.5	975.8	63.8	92.5	182.5

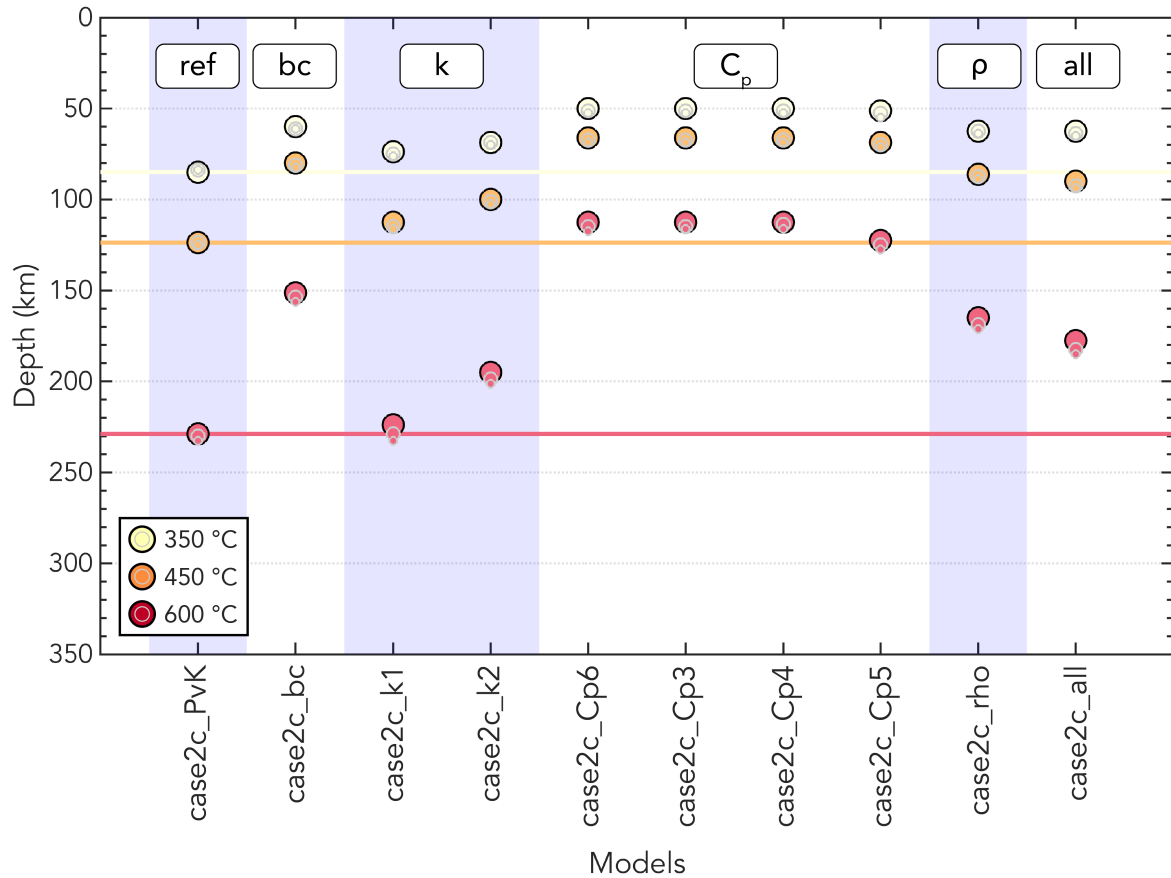


Figure S29: Change in maximum isotherm depth within the slab for models with different variations of temperature-dependent thermal parameters and the oceanic crust parameterisation within the slab (Table 1). The three isotherm depths plotted here are the same as the ones from the model diagnostics in Tables 2 and S1. Large black circles indicate the models including the oceanic crust parameterisation in the slab and the parameterisation of the continental overriding plate ($_{cp}$). Medium-sized grey circles indicate the $_{op}$ models including the parameterisation for an oceanic upper plate. Small grey circles indicate models $_{mc}$ without an overriding plate (but still including the oceanic crust parameterisation in the slab). Different groups of models (i.e., testing different functions for the temperature-dependence of the thermal conductivity k) are indicated by vertical bands for clarity. Here, 'ref' refers to the reference model case2c_PvK. Horizontal coloured lines highlight the reference values of model case2c_PvK_cp for easy comparison.

References used in the supplementary material

- Batchelor, G., 1967. An introduction to fluid dynamics. Cambridge university press.
- Berman, R.G., 1988. Internally-consistent thermodynamic data for minerals in the system $\text{Na}_2\text{O}-\text{K}_2\text{O}-\text{CaO}-\text{MgO}-\text{FeO}-\text{Fe}_2\text{O}_3-\text{Al}_2\text{O}_3-\text{SiO}_2-\text{TiO}_2-\text{H}_2\text{O}-\text{CO}_2$. *Journal of petrology* 29, 445–522.
- Berman, R.G., Aranovich, L.Y., 1996. Optimized standard state and solution properties of minerals: I. Model calibration for olivine, orthopyroxene, cordierite, garnet, and ilmenite in the system $\text{FeO}-\text{MgO}-\text{CaO}-\text{Al}_2\text{O}_3-\text{TiO}_2-\text{SiO}_2$. *Contributions to Mineralogy and Petrology* 126, 1–24.
- Bouhifd, M.A., Andrault, D., Fiquet, G., Richet, P., 1996. Thermal expansion of forsterite up to the melting point. *Geophysical Research Letters* 23, 1143–1146.
- Hofmeister, A., 1999. Mantle values of thermal conductivity and the geotherm from phonon lifetimes. *Science* 283, 1699–1706.
- van Keken, P.E., Currie, C., King, S.D., Behn, M.D., Cagnioncle, A., He, J., Katz, R.F., Lin, S.C., Parmentier, E.M., Spiegelman, M., et al., 2008. A community benchmark for subduction zone modeling. *Physics of the Earth and Planetary Interiors* 171, 187–197.
- McKenzie, D., Jackson, J., Priestley, K., 2005. Thermal structure of oceanic and continental lithosphere. *Earth and Planetary Science Letters* 233, 337–349.
- Xu, Y., Shankland, T.J., Linhardt, S., Rubie, D.C., Langenhorst, F., Klasinski, K., 2004. Thermal diffusivity and conductivity of olivine, wadsleyite and ringwoodite to 20 GPa and 1373 K. *Physics of the Earth and Planetary Interiors* 143, 321–336.